

# Development of Processing Maps and Constitutive Relationship for Thermomechanical Processing of Aluminum Alloy AA2219

S.V.S. Narayana Murty, Aditya Sarkar, P. Ramesh Narayanan, P.V. Venkitakrishnan, and J. Mukhopadhyay

(Submitted November 4, 2016; in revised form March 8, 2017; published online April 11, 2017)

Isothermal uniaxial compression tests were conducted on aluminum alloy AA2219 to study the evolution of microstructure over a wide range of temperatures (300–500 °C) and strain rates (0.001–100 s<sup>-1</sup>) with a view to study the flow behavior and concurrent microstructural evolution. True stress-true strain curves showed only a gradual flow softening at all temperatures except at 300 °C where strain hardening was followed by severe flow softening. Processing map delineating the stable ‘safe’ and unstable ‘unsafe’ regions during hot working is developed and validated by comparing the microstructures observed in the deformed compression specimens. Optimum processing parameters (temperature 450 °C and strain rate 0.001 s<sup>-1</sup>) for hot deformation of AA2219 were proposed based on contour maps of efficiency of power dissipation and strain rate sensitivity parameter. The activation energy value ( $Q_{\text{avg}}$ ) of AA2219 for hot working was computed to be 169 kJ/mol. Finally, a constitutive equation for hot working of AA2219 was established as:  $\dot{\epsilon} = 4.99 \times 10^9 \cdot \exp(0.06149\sigma) \cdot \exp(-168.958/RT)$ .

**Keywords** activation energy, aluminum alloy AA2219, constitutive equation, hot workability, processing maps

## 1. Introduction

2xxx series aluminum alloys are the material of choice for fabrication of aerospace structures owing to the combination of high strength, high toughness and damage tolerance they possess (Ref 1–3). Among the 2xxx Al alloys, Al-Cu-Mn (AA2219) alloy is utilized primarily in manufacture of cryogenic stage propellant tanks. This alloy possesses excellent mechanical properties at liquid hydrogen (fuel, boiling point 20 K) and liquid oxygen (oxidizer, boiling point 90 K) temperatures. Propellant tanks are fabricated by welding together the plates/sheets with rings/domes. These semi-products, plates, sheets and rings are realized through thermomechanical processing of direct chill cast billets of the alloy. Thermomechanical processing is used not only to impart the dimensional changes but also to impart the desired microstructural changes resulting in required mechanical properties (Ref 4–6).

Thermomechanical processing in the ‘unstable’ region can lead to flow localization/fracture leading to rejection of material during quality inspection. Therefore, optimization of bulk hot workability is of paramount importance in view of the economical and technical aspects involved. In recent years,

process modeling techniques have been commonly used to foresee the possibility of flow localization which can lead to fracture during hot working of materials (Ref 7, 8).

Modeling of thermomechanical processing is a powerful tool that aids in taking important decisions concerned with setting of the initial process parameters. One of the requirements for modeling of any hot deformation process is the knowledge of material flow behavior over a range of temperatures and strain rate regimes. The alloy behavior when subjected to hot working is represented through processing maps that demarcate ‘safe’ and ‘non-safe’ working regimes (Ref 9, 10). The processing conditions for stable and unstable deformation are denoted in these maps on axes of temperature and strain rate. Constitutive equations expressing flow stress as a function of process parameters ( $\epsilon$ ,  $\dot{\epsilon}$  and  $T$ ) are utilized for modeling any thermomechanical processing technique. These equations permit the extrapolation of stress data to strain rates experienced in any hot working operation on the shop floor that are beyond the laboratory test capabilities (Ref 11, 12). Therefore, understanding the constitutive alloy flow behavior under the conditions as encountered during hot working is important to exploit the benefits of processing techniques. In process modeling of any metal working operation through finite element analysis, it is essential to input a constitutive equation to obtain the flow stress values at any given location in the work piece.

In the study of hot workability of materials, it is a standard practice to conduct hot compression testing in fixed intervals of temperature (such as 50 °C intervals in the range of 0.5–0.8  $T_m$ ) and in the strain rates (in the range of 10<sup>-3</sup>–10<sup>2</sup> s<sup>-1</sup>) experienced in different metal working operations. This ensures the usefulness and applicability of the generated processing maps for any thermomechanical working operation. Further, the laboratory generated test data can be represented through a constitutive equation suitable for input in the finite element analysis software. These relationships are also useful in estimating the parameters such as stress exponent ( $n$ ), activa-

S.V.S. Narayana Murty, P. Ramesh Narayanan, and P.V. Venkitakrishnan, Materials and Mechanical Entity, Vikram Sarabhai Space Center, Trivandrum 695 022, India; and Aditya Sarkar and J. Mukhopadhyay, Department of Materials Science and Engineering, Indian Institute of Technology, Gandhinagar 382 424, India. Contact e-mails: susarla.murty@gmail.com and narayanamurty\_susarla@vssc.gov.in.

tion energy for hot working ( $Q$ ), temperature-compensated strain rate ( $Z$ ) which give an insight into the material behavior at elevated temperatures.

AA2219 is a widely used material for aerospace structures, yet few efforts have been made to study its constitutive flow behavior (Ref 1, 13). In order to obtain a desired microstructure with repeatable mechanical properties in the thermomechanically processed materials, it is essential to study the alloy behavior and to represent it using processing maps for the process metallurgist concerned with designing the process. Hence, this paper attempts to not only study the constitutive behavior of AA2219 but also to construct the deformation maps of the same since there is no reported literature correlating the two.

Therefore, the aim of the present study is to (a) generate high temperature stress-strain curves as a function of temperature and strain rate and (b) to construct processing maps for optimization of hot workability providing better microstructure control and (c) the constitutive relationship for the hot deformation of aluminum alloy AA2219.

## 2. Experimental Details

The raw material AA2219 (6.3Cu-0.3Mn-0.3Fe-0.2Si-0.18Zr-0.06Ti-0.1V and balance aluminum, all in wt.%) was in the form of a hot rolled plate of 40 mm thickness heat-treated to T87 temper. The microstructure of starting material consisted of coarse grains elongated in the rolling direction (RD) as shown in Fig. 1.

Hot compression test specimens with 10 mm diameter and 15 mm height were machined for compression testing from as-received hot rolled plate. Machining was done such that compression axis coincided with the RD. The cylinder edges were chamfered to prevent fold over during the initial stage of compression test. Flat surfaces of the cylinders were provided with concentric grooves to ensure lubrication while testing. The lubricant used was borosilicate glass. A thermocouple was implanted in a 0.8-mm hole drilled at half the specimen height

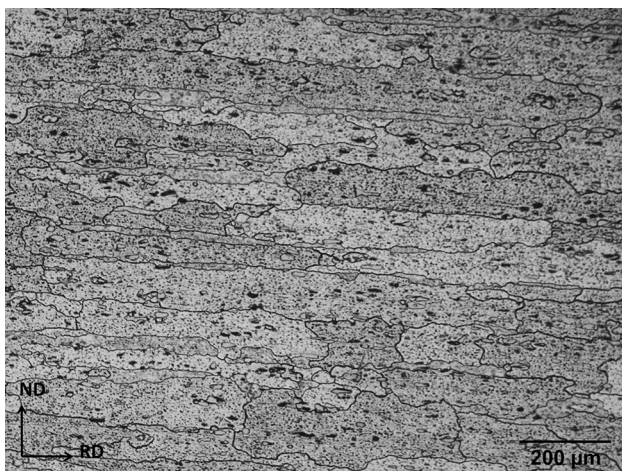


**Fig. 1** Optical photomicrograph of the initial microstructure of AA2219-T87 plate used in the present study. The plate rolling and normal directions are shown. The microstructure consists of grains with clear grain boundaries that are slightly elongated in the direction of rolling

to monitor the temperature. Hot uniaxial compression was carried out in a servo-hydraulic testing machine at constant true strain rates of  $0.001$ - $100 \text{ s}^{-1}$ . The entire assembly of the specimen, platens and push rods was heated to the testing temperature in a resistance furnace. Compression tests were performed over the temperature range  $300$ - $500 \text{ }^\circ\text{C}$  with an interval of  $50 \text{ }^\circ\text{C}$  between successive testing temperatures. The temperature control attained was  $\pm 2 \text{ }^\circ\text{C}$ . Tests were carried out to cause a 50% reduction in the initial height; the load-stroke curves of which were converted to true stress-true strain curves.

For microstructural observations, hot compression tested cylinders were cut along the center as per the sectioning plan shown in Fig. 2. Further the mechanical polishing of sectioned samples was done using emery papers of varying grit sizes (220-800) with water. Subsequently, the specimens were polished to a mirror surface using alumina ( $0.3 \text{ }\mu\text{m}$ ) paste and  $0.5 \text{ }\mu\text{m}$  diamond paste. The freshly polished specimens were etched with Keller's reagent (2 mL HF, 3 mL HCl, 5 mL  $\text{HNO}_3$  and 190 mL  $\text{H}_2\text{O}$ ). The etched specimens were observed, and photomicrographs were recorded using an Olympus GX 71 metallurgical microscope. The microstructures were recorded at the center of the sectioned plane of the cut cylinders as shown in the sectioning plan (Fig. 2).

## 3. Theoretical Considerations

### 3.1 Modeling of Dynamic Material Behavior Through Processing Maps

Processing maps are representations of alloy behavior in terms of its microstructural evolution under different sets of process parameters such as  $\epsilon$ ,  $\dot{\epsilon}$  and  $T$ . They consist of power dissipation map, strain rate sensitivity contour map and an

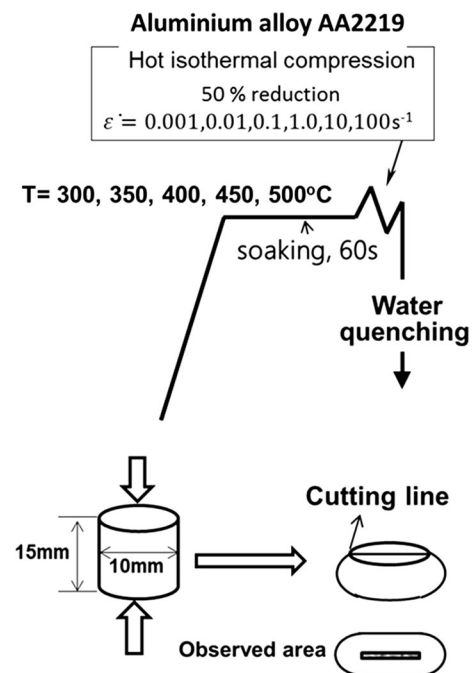


**Fig. 2** Schematic of the experimental plan (with heating, soaking, deformation and cooling sequence) adopted in the present study. The sectioning plan for microstructural observation is also shown

instability map. Instability in metal flow (for example, localized flow, adiabatic shear or cracking) is observed if the rate of entropy production in an alloy system does not constitutively match with the rate of entropy input by imposed process conditions. The dynamic material model (DMM) was developed by Prasad et al. (Ref 9) which considered the work piece as a dissipator of power.

The total power dissipated by the workpiece is given as

$$P = \sigma \dot{\epsilon} = \int_0^{\dot{\epsilon}} \sigma d\dot{\epsilon} + \int_0^{\sigma} \dot{\epsilon} d\sigma = G + J \quad (\text{Eq 1})$$

The first integral ( $G$ ) in Eq 1 is the power input dissipated simply as a rise in temperature while the second integral ( $J$ ) gives the power dissipated by metallurgical processes and its relationship with  $G$  is given by

$$\frac{dJ}{dG} = \frac{\dot{\epsilon} d\sigma}{\sigma d\dot{\epsilon}} = \frac{d(\ln \sigma)}{d(\ln \dot{\epsilon})} = m(\text{strain rate sensitivity}) \quad (\text{Eq 2})$$

Deformation of an alloy should be ideally carried out in regions that exhibit maximum efficiency of power dissipation ( $\eta$ ), except when microstructural inhomogeneities occur.  $\eta$  is given by the equation:

$$\eta = \frac{J}{J_{\max}} = \frac{2m}{m+1} = \frac{2J}{P} \quad (\text{Eq 3})$$

Locations of microstructural instability are predicted on the principles of maximum rate of entropy production (Ref 14, 15) and is found by plotting the instability parameter  $\xi(\dot{\epsilon})$  given by

$$\xi(\dot{\epsilon}) = \frac{\partial \ln[m/(m+1)]}{\partial \ln \dot{\epsilon}} + m < 0 \quad (\text{Eq 4})$$

Negative value of instability parameter  $\xi(\dot{\epsilon})$  indicates that the material flow is unstable in that particular region. The efficiency of power dissipation ( $\eta$ ) as seen in Eq 3 represented exclusively as a function of the strain rate sensitivity parameter ( $m$ ) holds true only when the ( $\sigma$ )–( $\dot{\epsilon}$ ) curve at any given  $\epsilon$  and  $T$  obeys the power law ( $\sigma = k\dot{\epsilon}^m$ ). For alloy systems that do not follow the power law relation, the computation of  $\eta$  in terms of  $m$  from Eq 3 and the flow instability condition given in Eq 4 becomes incorrect.

Therefore, a modified DMM approach proposed by Narayana Murty et al. (Ref 15-20) has been used in the present study as it can be used for all types of flow stress–strain relationship. In this approach, the condition for the metallurgical instability is given as

$$\xi = \frac{mP}{J} - 1 = \frac{2m}{\eta} - 1 < 0 \quad (\text{Eq 5})$$

which can also be written as  $2m < \eta$ .

For materials insensitive to strain rate changes, i.e.,  $m \rightarrow 0$  or  $J = 0$ . As  $J = 0$ ,  $G = P$  and the entire power input would only dissipate as heat leading to plastic instability by a continuum process such as adiabatic shearing. Hence,

$$J = 0 \Rightarrow \eta = 0 \quad (\text{Eq 6})$$

From Eq 5 and 6, the condition for metallurgical instability for materials exhibiting any type of flow stress distribution can be written as

$$2m < \eta \leq 0 \quad (\text{Eq 7})$$

The instability criterion (Eq 7) is valid for any type of  $\sigma - \epsilon$  curve. For a material whose stress-strain curve follows the power law,  $\eta = 2m/(m+1)$ , which is always less than  $2m$  for  $0 < m \leq 1$ , and hence, the material flow is stable.

### 3.2 Modeling of Hot Deformation by Constitutive Analysis

**3.2.1 Types of Constitutive Equations.** Thermomechanical processing of a material involves hot working operations such as rolling, forging and extrusion. Hot workability is the ability of a material to be deformed under conditions of high temperature (greater than  $0.6 T_m$  where  $T_m$  is the absolute melting temperature in degrees Kelvin) and relatively high strain rates ( $10^{-1}$ – $10^2 \text{ s}^{-1}$ ) (Ref 21, 22). Hence, the field of hot working appears to be similar creep as both share identical temperature ranges that involve thermally activated mechanisms (Ref 12). The primary difference between creep and hot working is the strain rate as hot working involves much higher strain rates as compared to those observed in creep. Hot working proceeds to very high strains as a result of the high strain rates with an objective of reducing the flow stress, whereas in creep there is a curtailment of total strain as a result of the low strain rates ( $10^{-2}$ – $10^{-6} \text{ s}^{-1}$ ) (Ref 23). Thus, the same relationships between stress, strain rate and temperature have been employed in both, i.e., creep and hot workability studies.

The constitutive equations used in hot workability studies and creep analysis include the following (Ref 12):

$$A_p \sigma^{n_p} = \dot{\epsilon} \exp(Q_p/RT) = Z_p(\text{power}) \quad (\text{Eq 8})$$

$$A_g (\sigma/G)^{n_g} = \dot{\epsilon} kT/(bGD_0(-Q_D/RT)) \quad (\text{Eq 9})$$

$$A_E \exp \beta \sigma = \dot{\epsilon} \exp(Q_E/RT) = Z_E \quad (\text{Eq 10})$$

$$A(\sinh \alpha \sigma)^n = \dot{\epsilon} \exp(Q/RT) = Z(\sinh) \quad (\text{Eq 11})$$

where  $A_p$ ,  $A_g$ ,  $A_E$ ,  $A$ ,  $\alpha$ ,  $\beta$ ,  $n_p$ ,  $n_g$ ,  $n_s$ ,  $D_0$ ,  $Q_p$ ,  $Q_D$ ,  $Q_E$  and  $Q$  are empirical constants,  $R$  is the gas constant,  $k$  is the Boltzmann constant,  $b$  is Bergers vector and  $G$  is the shear modulus (Ref 12).

The activation energy ' $Q$ ' of a mechanism is generally derived from an Arrhenius plot ( $\ln[\sinh(\alpha\sigma)]$  versus  $1000/T$ ) in a linear range. The procedure adopted for computation for  $A$ ,  $n$  and  $Q$  parameters from the Arrhenius plot has been explained in the succeeding section in detail. The aforementioned parameters differ to some extent for the same set of data due to difference in microstructures evolved at different temperature or strain rate regimes of hot working or creep (Ref 12). The values of activation energy in creep ( $Q_p$ ) are usually similar to that of self-diffusion ( $Q_D$ ) while the activation energy values in hot working ( $Q_{HW}$ ) are often much larger as the microstructure does not remain constant and evolves rapidly at different strain rates during hot working (Ref 12, 23).

As seen from Eq 10, the parameter  $n_p$  varies with stress. At high stress levels as observed in conventional hot working operations, the  $n_p$  values attain large values which lead to the power law breakdown. Hence, the power law is only preferred in creep analysis where low stress levels are observed as compared to hot working conditions (Ref 23). Though the exponential law was favored over the power law for hot working analysis, it was later found to break down at

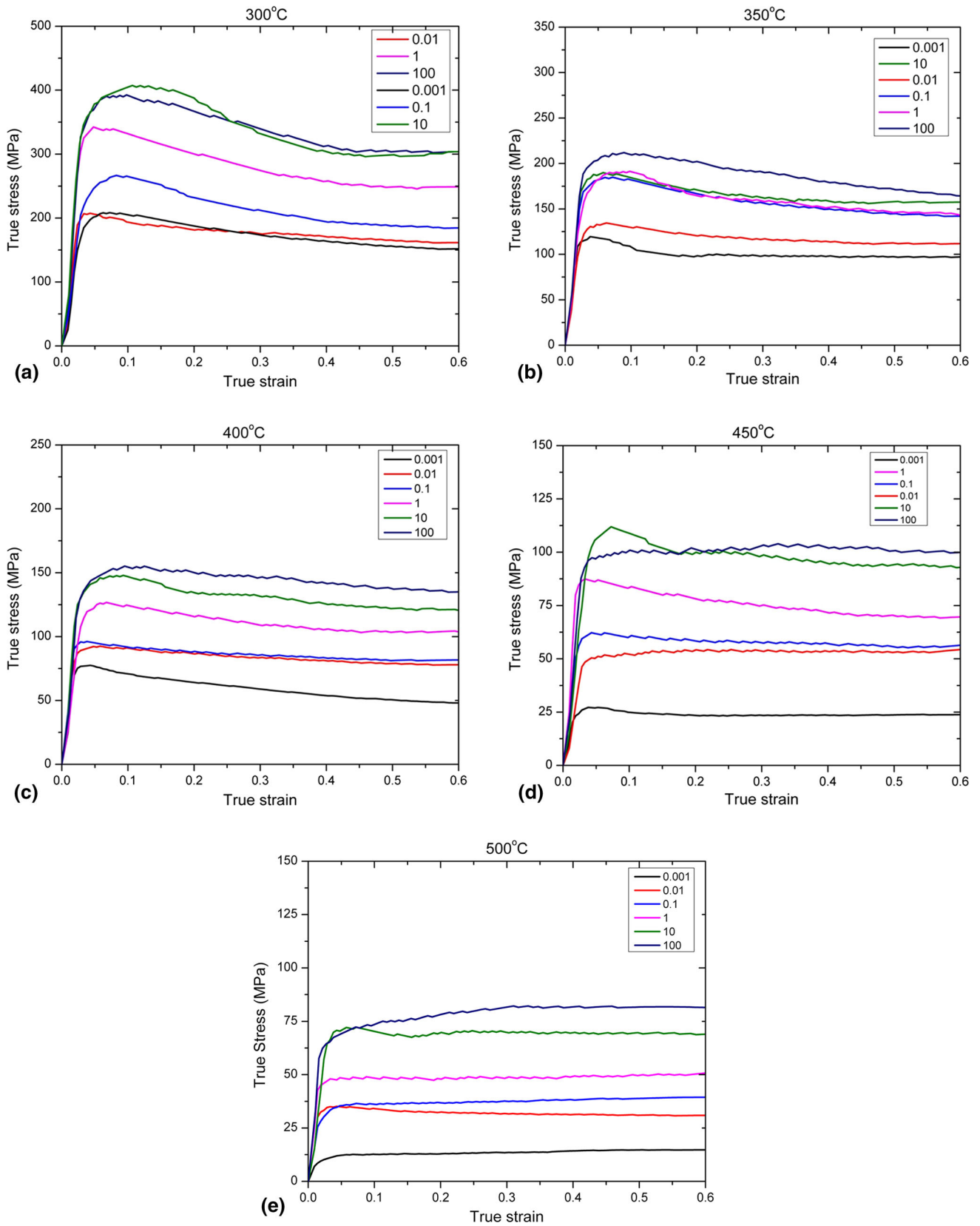


**Fig. 3** (a–e): True stress–true strain curves obtained from the hot isothermal uniaxial compression testing of AA2219-T87 specimens at different temperatures and strain rates

high temperatures and low strain rates (below  $1 \text{ s}^{-1}$ ) (Ref 23). Therefore, a more general relation (Eq 11) covering a wide range of stresses encountered during both creep and hot working processes was established (Ref 21-23). The hyperbolic sine law (Eq 11) usually remains linear over a broad range where the stress multiplier ' $\alpha$ ' is taken as the ratio ( $\beta/n_p$ ) since the sinh law approximates exponential law (Eq 10) at high  $\sigma$  levels and the power law (Eq 8) at low  $\sigma$  levels.

**3.2.2 Physical Significance of Activation Energy.** The activation energy for hot working ( $Q_{HW}$ ) points to the degree of difficulty in hot deforming a material (Ref 24, 25) and is derived from hyperbolic sine law proposed by Sellars and McG. Tegart as seen from Eq 11. In case of high stacking fault energy (SFE) materials (for example aluminum and its alloys), dynamic recovery is the dominant softening mechanism (Ref 26). Hence, the  $Q_{HW}$  of an aluminum alloy represents mainly the free energy barrier to dislocation slipping on slip planes. For aluminum alloys, the  $Q_{HW}$  values generally increase as the volume fraction of alloying elements increases. This increase in  $Q_{HW}$  represents the resistance to softening due to the retardation in DRV by fine, coherent dispersoids such as  $\text{Al}_3\text{Zr}$  in AA2219 due to Zr addition (Ref 12, 24). At elevated temperatures, the dispersoids play no role in pinning the dislocations (Ref 27). In such cases, the hot working activation energy remains fairly same over a varied range of strain rates. If approximately the same value of  $Q_{HW}$  is found over many orders of magnitude of strain rate, then the average value is taken over a variety of applied hot deformation conditions (Ref 22)

## 4. Results and Discussion

### 4.1 Flows Stress Behavior

Flow stress curves acquired while deforming a material at high temperatures indicate any one of the following two types of material behavior, viz. (a) resulting from dynamic recrystallization (DRX) and (b) dynamic recovery (DRV). Appearance of new grains due to DRX causes softening which leads to decrease in work hardening leading to a pronounced stress peak. Subsequently, a further increase in strain causes a reduction in the flow stress until steady state, i.e., balance between strain hardening and flow softening is attained (Ref 26). Hence, in case of DRX, the stress-strain curve is divided into four regions depending on the micromechanism dominant during a particular stage in hot working. In stage I, the pile up of dislocations leads to strain hardening. During stage II, the hardening caused due to increase in applied strain and softening caused by either DRV or DRX compete with each other. In stage III, there is a sudden drop in the flow stress as a result of the dominance of flow softening due to DRX over work hardening. Stage IV is stabilization of the flow stress leading to a steady state (Ref 28). Metals and alloys of low to medium SFE show such a four-stage flow curves as DRX is the primary softening mechanism in them during hot deformation (Ref 26).

A second type of high temperature deformation behavior exists where the strain hardening rate only gradually decreases with increasing deformation. Further, the rate of strain hardening eventually approaches zero at high strains leading to a

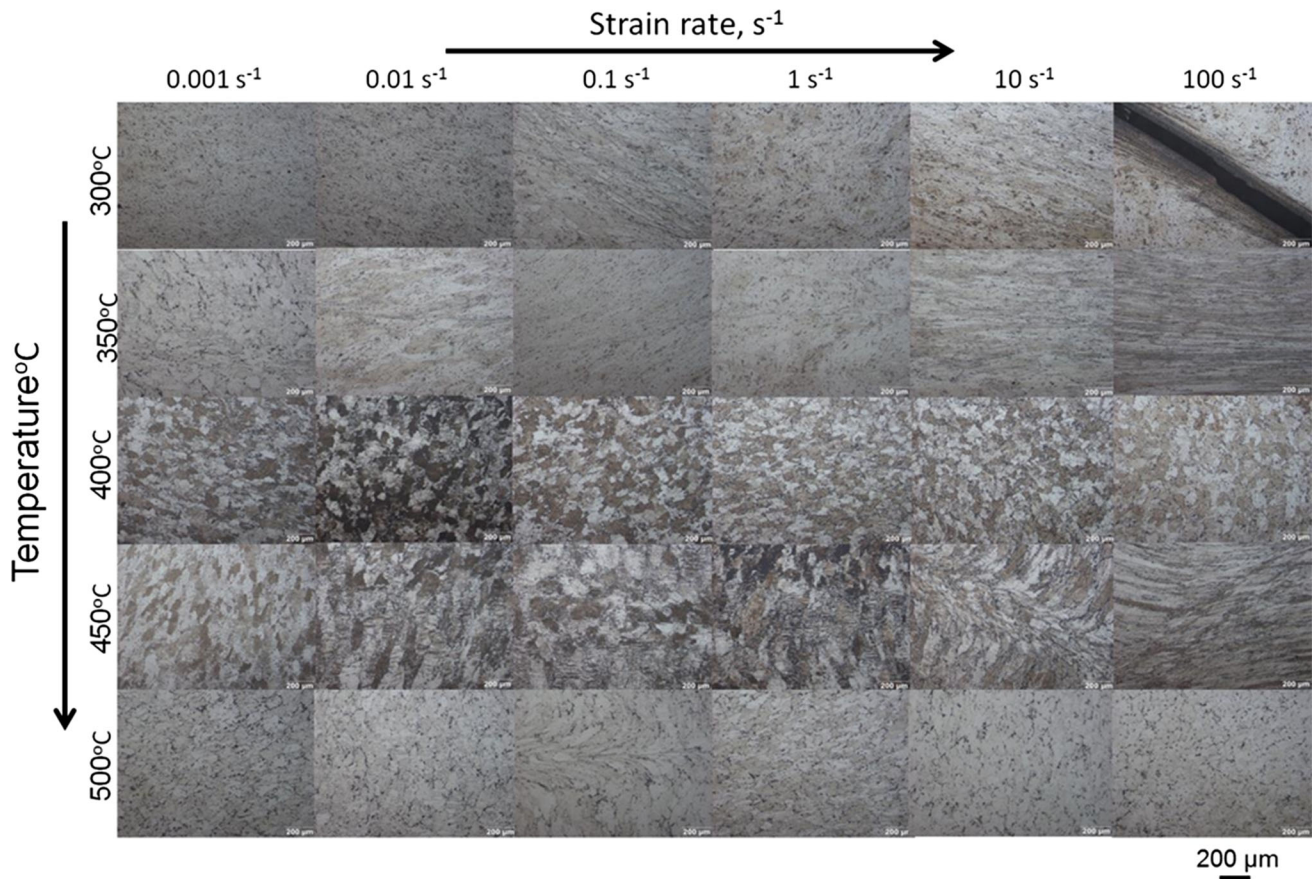


**Fig. 4** Optical microstructures of the hot compression tested specimens deformed at different temperatures and strain rates

**Table 1 Microstructural observations in plane strain compressed specimens at different strains tested at different temperatures and strain rates**

Temperature	Strain rate					
	0.001 s <sup>-1</sup>	0.01 s <sup>-1</sup>	0.1 s <sup>-1</sup>	1 s <sup>-1</sup>	10 s <sup>-1</sup>	100 s <sup>-1</sup>
300 °C	Deformed grain structure with no clear boundaries	Compressed grains indicative of only a recovered microstructure	Compressed grains; flow localization is also observed	Deformed grain structure with deformation bands within the boundaries	Compressed grains with some localization of flow	Cracking due to severe flow localization
350 °C	Deformed grain structure with deformation bands within the boundaries	Flow localization resulting in a shear band	Localized flow along with shear banding	Flow localization along with shear banding	Severe flow localization resulting in shear banding	Highly compressed grain structure with severe flow localization
400 °C	Reconstituted equiaxed microstructure with wavy grain boundaries	Reconstituted equiaxed structure, visibly different from the initial elongated grain structure	Reconstituted equiaxed microstructure with wavy grain boundaries	Reconstituted equiaxed microstructure indicating stable flow	Reconstituted equiaxed microstructure with wavy grain boundaries	Equiaxed coarse grain structure with some deformation bands within the boundaries
450 °C	Reconstituted microstructure exhibiting equiaxed grains	Partly reconstituted grain structure with deformation bands within elongated boundary	Deformation bands existing within elongated boundaries	Deformation bands existing within elongated boundaries	Severe flow localization resulting in kinking of grain boundaries	Severe flow localization resulting in kinked grain boundaries
500 °C	Equiaxed grain structure with mostly coarse grains	Partly reconstituted microstructure exhibiting equiaxed grains	Flow localization leading to shear banding	Fully reconstituted structure with slightly compressed fine grains	Partly reconstituted microstructure with fine subgrains visible within coarse grains	Fully reconstituted structure with fine equiaxed grains

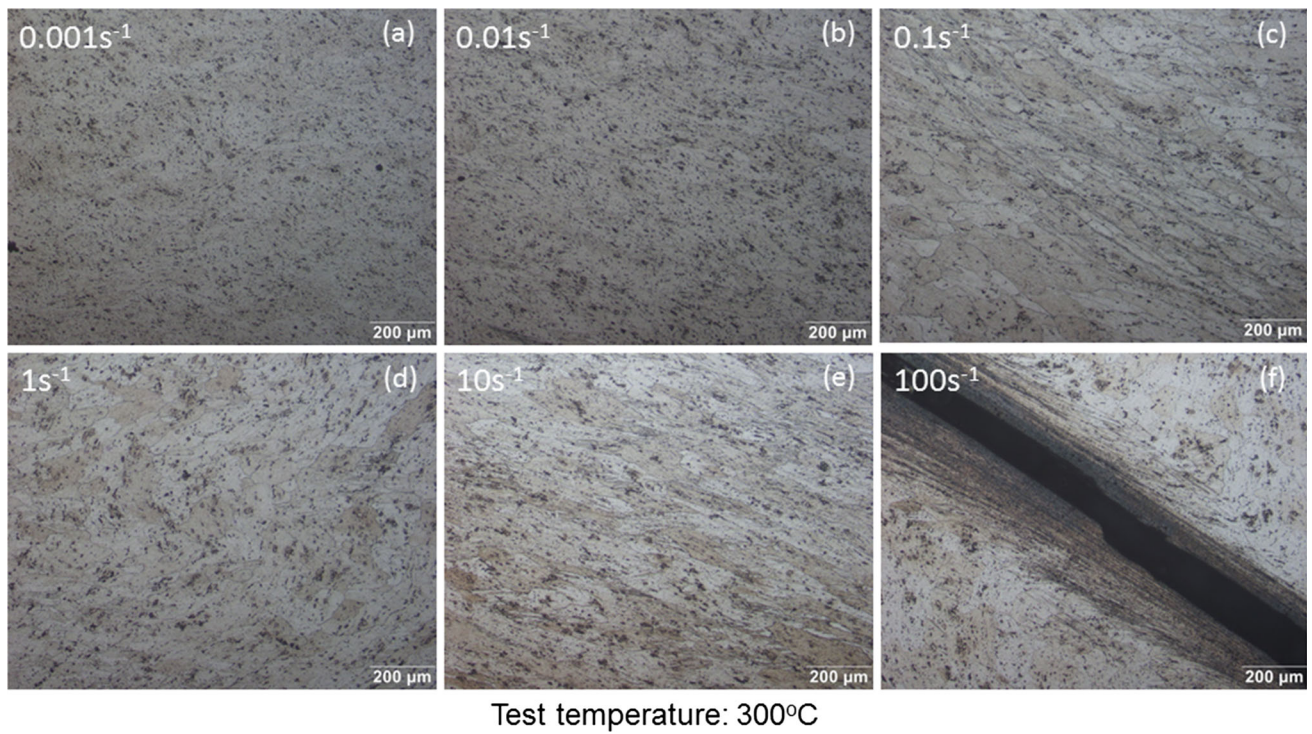


**Fig. 5** Optical microstructures of the hot compression tested specimens deformed at 300 °C and strain rates of (a)  $0.001 \text{ s}^{-1}$ , (b)  $0.01 \text{ s}^{-1}$ , (c)  $0.1 \text{ s}^{-1}$ , (d)  $1 \text{ s}^{-1}$ , (e)  $10 \text{ s}^{-1}$  and (f)  $100 \text{ s}^{-1}$

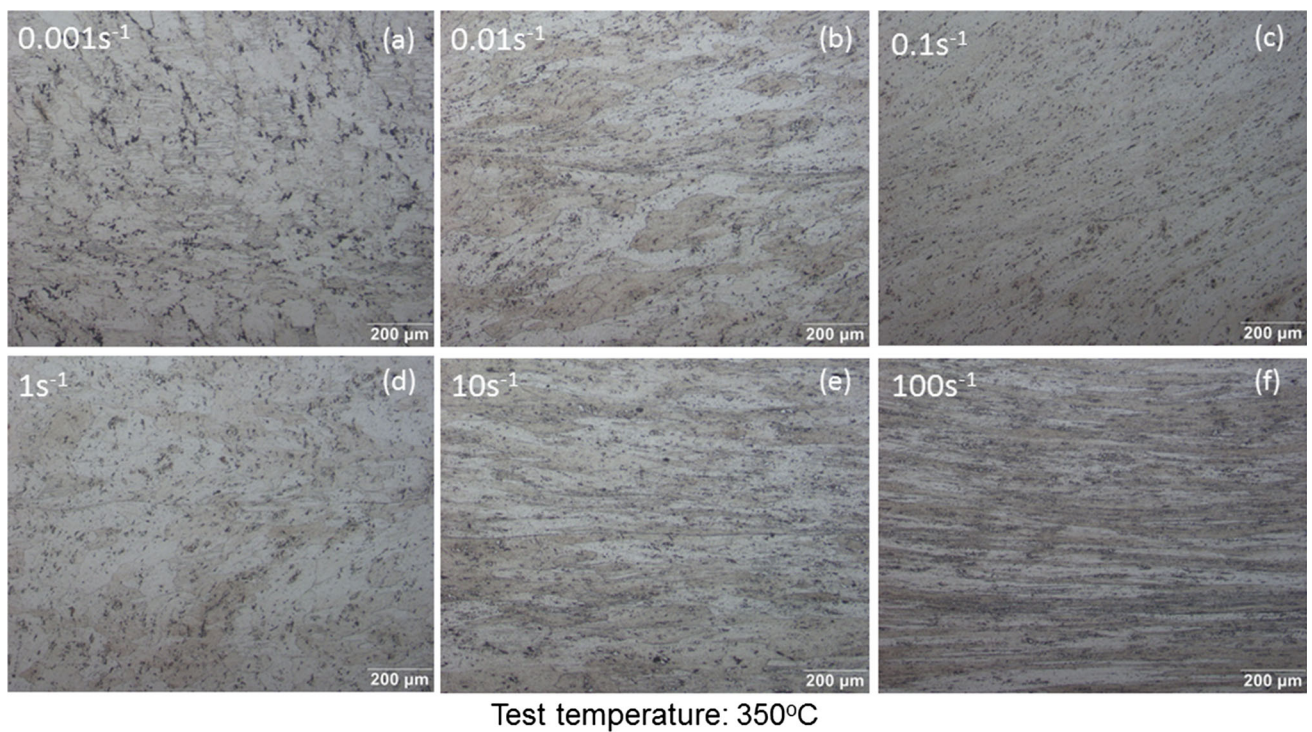


**Fig. 6** Optical microstructures of the hot compression tested specimens deformed at 350 °C and strain rates of (a)  $0.001 \text{ s}^{-1}$ , (b)  $0.01 \text{ s}^{-1}$ , (c)  $0.1 \text{ s}^{-1}$ , (d)  $1 \text{ s}^{-1}$ , (e)  $10 \text{ s}^{-1}$  and (f)  $100 \text{ s}^{-1}$

steady state of flow. This type of behavior is characterized by the absence of a clear stress peak as observed for a material with low to medium SFE. DRV is responsible for such gradual softening behavior characterized by the absence of a clear stress

peak. Here, the steady-state flow is achieved when the rate of DRV approaches the strain hardening rate leading to balance between the two (Ref 26). This implies that the extent of softening in DRV-type materials is less as compared to the

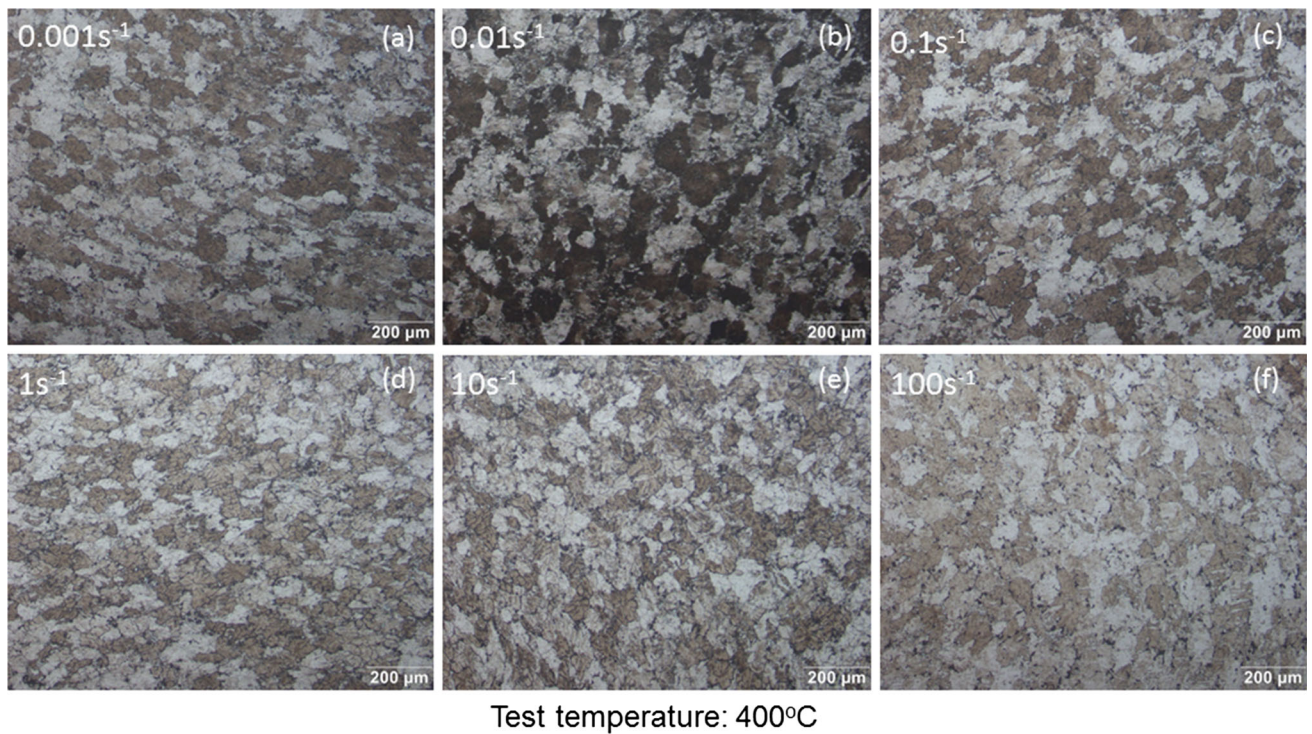


**Fig. 7** Optical microstructures of the hot compression tested specimens deformed at 400 °C and strain rates of (a) 0.001 s<sup>-1</sup>, (b) 0.01 s<sup>-1</sup>, (c) 0.1 s<sup>-1</sup>, (d) 1 s<sup>-1</sup>, (e) 10 s<sup>-1</sup> and (f) 100 s<sup>-1</sup>

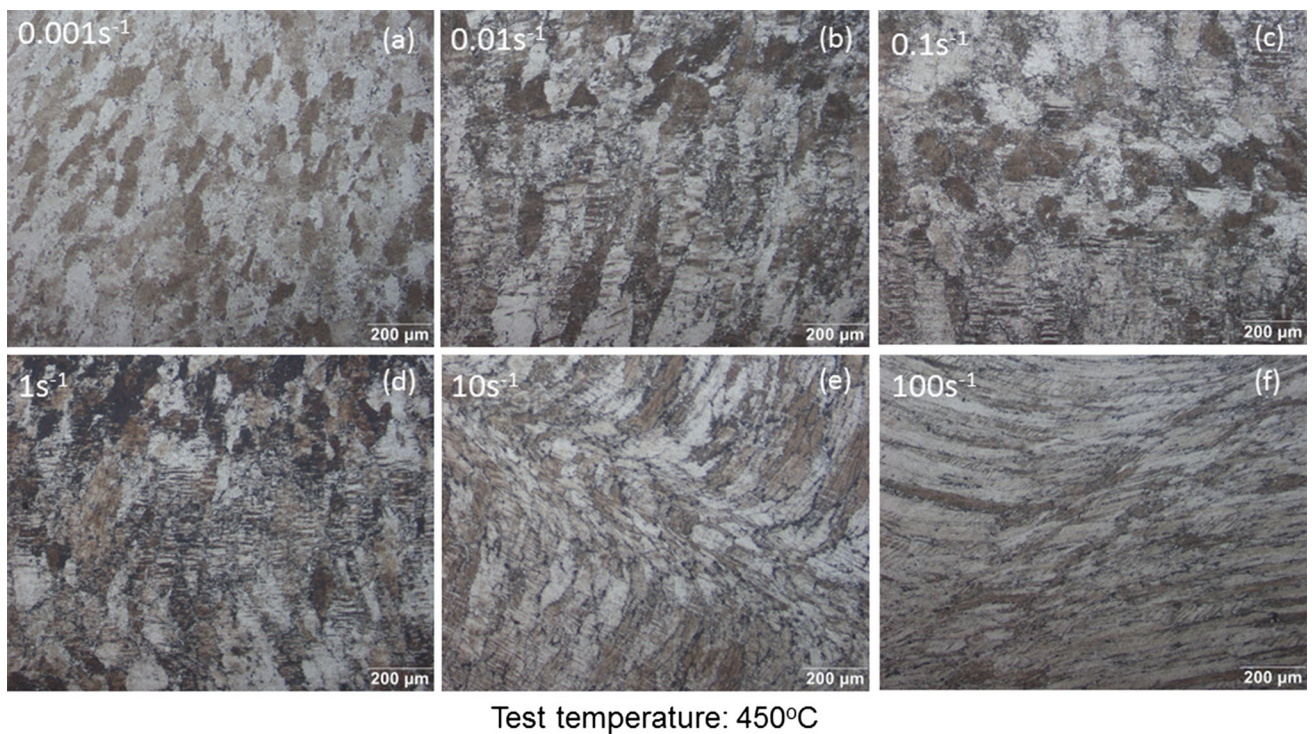
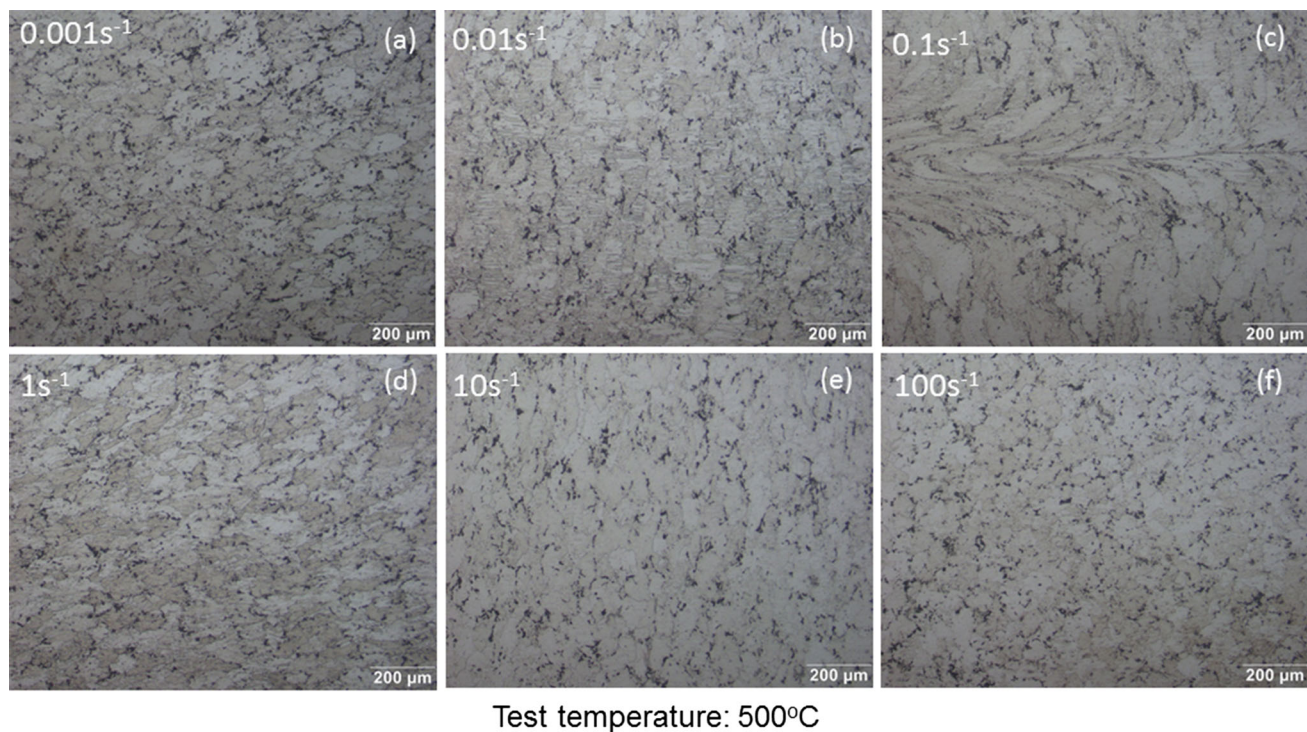


**Fig. 8** Optical microstructures of the hot compression tested specimens deformed at 450 °C and strain rates of (a) 0.001 s<sup>-1</sup>, (b) 0.01 s<sup>-1</sup>, (c) 0.1 s<sup>-1</sup>, (d) 1 s<sup>-1</sup>, (e) 10 s<sup>-1</sup> and (f) 100 s<sup>-1</sup>

DRX type materials. Flow curves indicating occurrence of DRV are exhibited by high SFE materials as these are prone to easy dislocation climb and cross-slip (Ref 29).

Figure 3(a-e) shows the true stress-true strain curves of AA2219 obtained in the present study. It can be observed that as with increase in testing temperature or decrease in the





Test temperature: 500°C

**Fig. 9** Optical microstructures of the hot compression tested specimens deformed at 500 °C and strain rates of (a) 0.001 s<sup>-1</sup>, (b) 0.01 s<sup>-1</sup>, (c) 0.1 s<sup>-1</sup>, (d) 1 s<sup>-1</sup>, (e) 10 s<sup>-1</sup> and (f) 100 s<sup>-1</sup>

applied strain rate, the flow stress monotonically decreases. The flow softening seen after the initial work hardening in all the flow curves (Fig. 3a-e) is due to the dominance of the softening mechanisms such as DRV and DRX over strain hardening. Flow softening is more conspicuous at low strain rates, evidenced by the appearance of a trough in the flow curves of samples deformed at strain rates of 0.001 and 0.01 s<sup>-1</sup> at all temperatures (except 500 °C) as shown in Fig. 3(a)-e).

Degree of flow softening observed in the flow curves obtained at 300 °C (Fig. 3a) is much more compared to that observed in the flow curves obtained at all other temperatures (Fig. 3b-e). This indicates occurrence of DRV as the principal restoration mechanism in samples deformed at all temperatures (except 300 °C) since they only show a gradual softening of their flow curves. The sudden and severe flow softening observed in Fig. 3(a) might be attributed to the flow localization explained in the succeeding sections.

#### 4.2 Microstructural Evolution

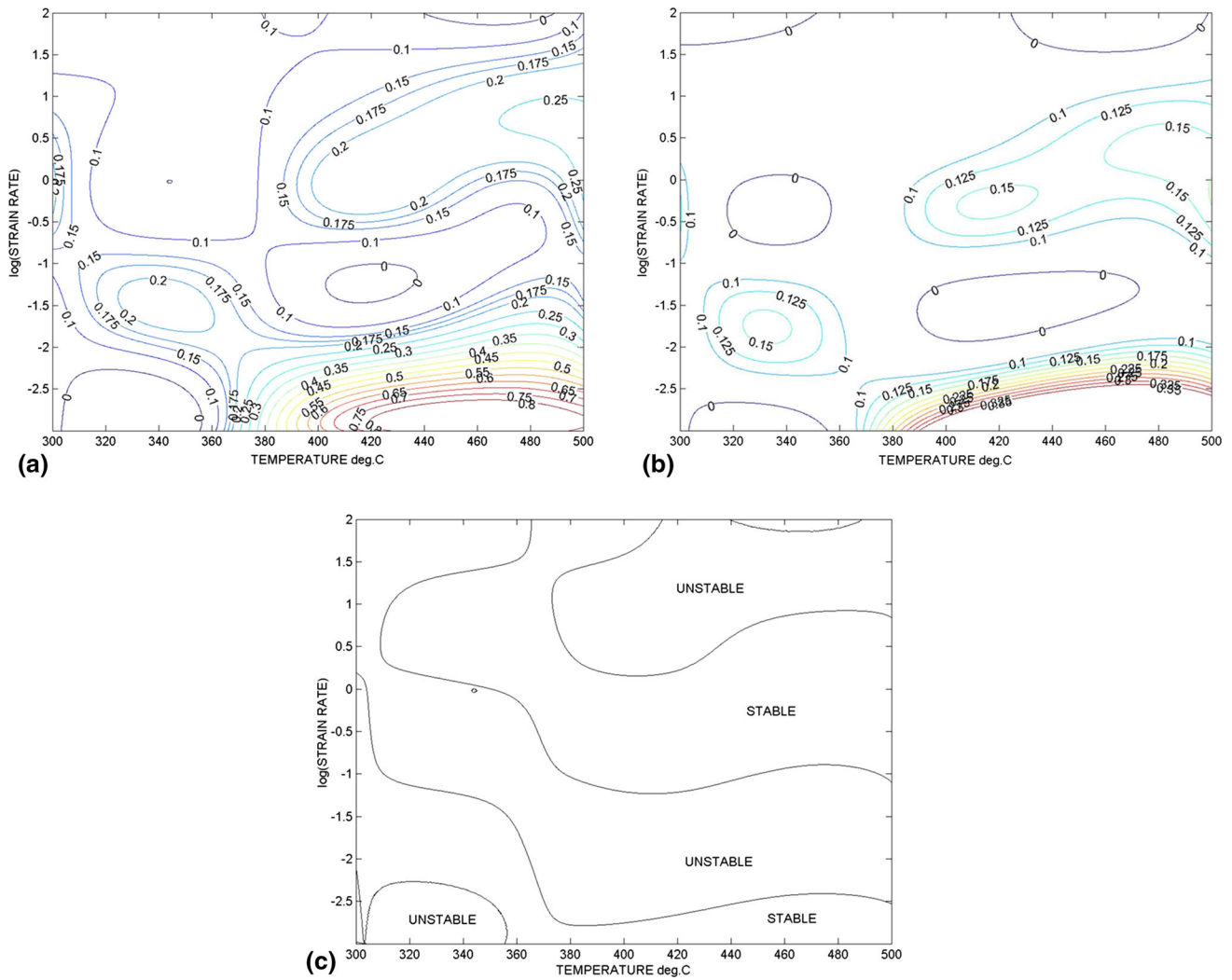
Figure 4 shows a palette of optical photomicrographs of the specimens hot compressed at different temperatures and strain rates. These belong to microstructures recorded at the center of the sectioned plane. Details of the microstructural observations in specimens at various temperatures and strain rates are presented in Table 1.

Figure 4 shows that as with an increase in the deformation temperature and a decrease in strain rate, there is an increase in the extent to which reconstitution of the original microstructure takes place. This is evidenced by the appearance of a fully reconstituted microstructure consisting of equiaxed grains at deformation temperatures of 400, 450, 500 °C (Fig. 7, 8 and 9). These microstructures are in stark difference compared to the initial elongated grain structure. The samples deformed at

300 °C are characterized only by a deformed grain structure at all strain rates, whereas the sample deformed at 100 s<sup>-1</sup> shows adiabatic shear banding leading to cracking (Fig. 5). The microstructures of samples deformed at 350 °C are characterized by flow localization at all strain rates except at 0.001 s<sup>-1</sup> where deformed grain structure with deformation bands within the boundaries was observed (Fig. 6). For the samples deformed at 400 °C, the microstructures are characterized by wavy grain boundaries at all strain rates (Fig. 7). At a deformation temperature of 450 °C, the samples deformed at strain rates in the range of 0.001-1 s<sup>-1</sup> exhibited partial reconstituted grain structure with deformation bands existing within the initial elongated boundaries, whereas the samples deformed at high strain rates of 10-100 s<sup>-1</sup> showed flow localization (Fig. 8).

#### 4.3 Generation of Processing Maps

In the present study maps of strain rate sensitivity ( $m$ ), efficiency of power dissipation and instability contour maps have been plotted for a strain of 0.5 and are presented in Fig. 10. These maps are constructed using Eq 1-7; the procedure for which has been discussed in detail elsewhere (Ref 20). Regions of unstable metal flow were identified from these plots using the Ziegler's continuum principles. Evolved microstructures were studied to further validate the information provided by the processing maps. To generate a processing map, it is important to input the experimental data, i.e., the flow stress as a function of temperature, strain rate and strain. The maps reveal two stable domains, viz. Domain I occurring at high temperature (370-500 °C) and low strain rates (0.001-0.01 s<sup>-1</sup>) and another Domain II at high temperature (370-500 °C) and high strain rates (0.32-10 s<sup>-1</sup>). In Domain 1, the maximum efficiency of power dissipation is 0.8 and corresponding  $m$



**Fig. 10** (a'') represents the efficiency of power dissipation ( $\eta$ ) map at  $\varepsilon = 0.5$ , (b'') represents contour map of strain rate sensitivity ( $m$ ) at  $\varepsilon = 0.5$ , (c'') represents the instability map for the alloy showing stable (safe) and unstable (unsafe) working zones at strains of  $\varepsilon = 0.5$

value is 0.35. Higher values of power dissipation indicate stable flow during hot deformation. In view of the high values of  $\eta$  and  $m$ , this region corresponds to the domain of superplasticity (Ref 30). Microstructural observations of the deformed specimens from this area reveal fully reconstituted grains of equiaxed nature with an apparent increase in the grain size with decreasing strain rate (Fig. 7a, b, 8a and 9a).

Domain 2 occurring in the high temperature and high strain rate range has a maximum efficiency of power dissipation of 0.3 and  $m$  value of 0.2. Microstructural observations of the deformed specimens from this domain reveal fully reconstituted grains of equiaxed nature with no apparent change in the grain size with varying strain rate as shown in Fig. 7(d), (e) and 9(d), (e). This region corresponds to the region of dynamic recovery.

Processing maps for AA2219 shown in Fig. 10 reveal flow instabilities in the temperature range of 300-350 °C in high strain rate regime (0.01-100 s<sup>-1</sup>). The instabilities are in the form of localized flow, and in extreme cases, flow localization led to cracking (300 °C and 100 s<sup>-1</sup>) (Fig. 6f). Further, the microstructures of the specimens deformed at 450 °C, 10 and 100 s<sup>-1</sup> revealed the presence of kinks. These microstructures are found to be well within the instability region of the processing map (Fig. 8e, f). Deformation bands within the

grains were noticed in the specimens deformed at 350 °C and 0.001 s<sup>-1</sup> and 450 °C and in the temperature range of 0.01-1 s<sup>-1</sup> (Fig. 6a and 8b-d).

Based on the above microstructural observations of various domains in the processing maps, the optimum hot deformation conditions for this alloy are  $T = 450$  °C, strain rate 0.001 s<sup>-1</sup>. Ideally, in the industry, the highest possible strain rates and least possible flow stresses are desired to maximize the productivity. Since optimum processing conditions occur at lower strain rates, deformation can still be carried out over a given range of temperatures (380-500 °C) and strain rates (0.3-10 s<sup>-1</sup>) to increase productivity.

#### 4.4 Constitutive Equation for Hot Deformation of AA2219

The flow stress behavior of a material influences the decision of selecting any one of the aforementioned equations (Eq 8-11) to construct a constitutive model for its hot working. In the case of high SFE metals such as aluminum, the flow curves exhibit declining strain hardening to attain a steady-state regime ( $\varepsilon_s$ ) due to DRV. Hence, for DRV-type materials, the steady-state stress is normally used for computation of  $Q_{HW}$  as there is the absence of a clear stress peak (Ref 12, 23). In case

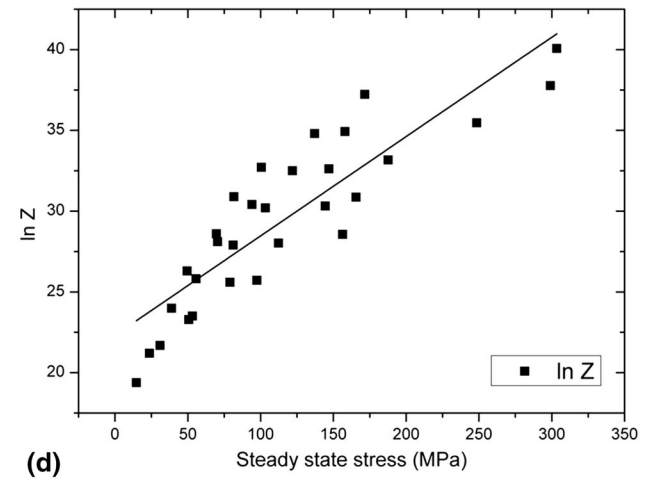
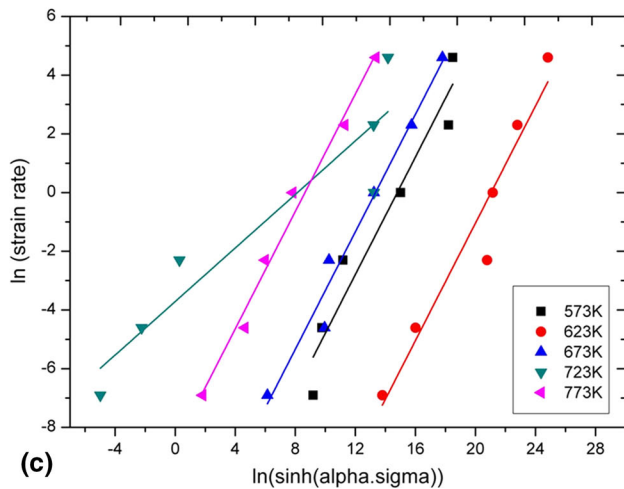
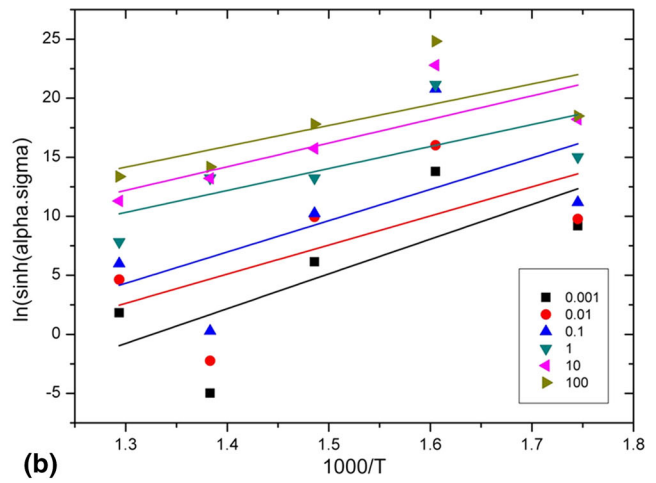
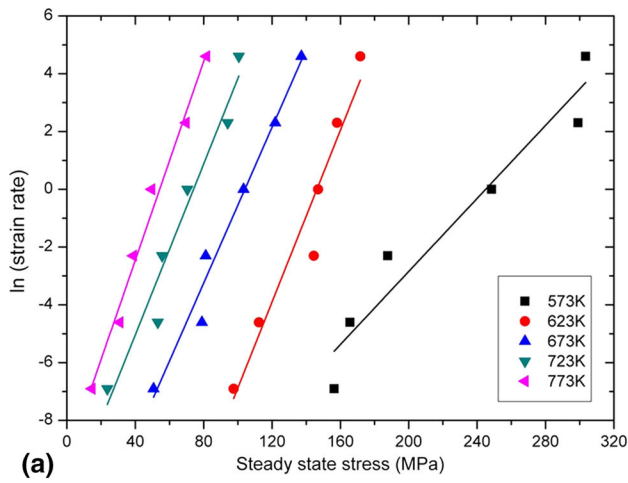


**Fig. 11** (a) Plot of  $\ln(\dot{\epsilon})$  vs. steady-state stress at various temperatures (slope of individual plot gives ' $\alpha$ ' for the alloy at that temperature), (b) relationship between steady state ( $\sigma_s$ ) and temperature ( $T$ ), (c) relationship between steady-state stress ( $\sigma_s$ ) and strain rate ( $\dot{\epsilon}$ ) and (d) relationship between and Zener-Holloman parameter ( $Z$ ) and steady-state stress ( $\sigma_s$ )

**Table 2** Values of material constants and activation energy for aluminum alloy AA2219

$A$	$\alpha$	$Q$ , kJ/mol
4.922E+09	0.06149	168.958

**Table 3** Activation energy values for different grades of aluminum alloys

Alloy	Condition	$Q$ , kJ/mol	References
2024	As cast	178	33
5456	Hot extruded	161	23
5182	Hot extruded	145	23
6061	Pre-aged (as cast)	205	23
5083	Hot extruded	172	23, 33
7075	As cast	145	34
7075	Extruded + precipitated	148	34
7075	Extruded + solutionized	205	34

of metals exhibiting DRV, both creep and hot working are similar with regard to the microstructural evolution observed as a function of stress and temperature (Ref 22). As Eq 10 was found to best describe the steady stress data at high stresses experienced during hot working operations (Ref 12, 22), it led us to the selection of the exponential law (Eq 10) to further construct the constitutive model for hot working of AA2219 which also exhibits DRV type of behavior.

**4.4.1 Procedure for Development of Constitutive Equations.** Constitutive equation relating flow stress to the principal processing parameters such as strain, strain rate and temperature has been developed from the hot isothermal compression test data obtained in the present study. As explained previously, the exponential law (where the constant  $\beta$  is analogous to the stress multiplier  $\alpha$  of the hyperbolic sine function) has been selected to construct a constitutive equation in the present study; the exponential law is as follows

$$A_E \exp \alpha \sigma = \dot{\epsilon} \exp(Q/RT) = Z_E(\text{exponential}) \quad (\text{Eq 12})$$

Here,  $A_E$  and  $\alpha$  are constants while  $Q$  is the activation energy for hot deformation.

**Table 4 Comparison between the calculated and measured flow stress values at strain of 0.5**

Strain rate	Temperature								
	573 K			623 K			673 K		
	Calculated stress, MPa	Measured stress, MPa	% error	Calculated stress, MPa	Measured stress, MPa	% error	Calculated stress, MPa	Measured stress, MPa	% error
0.01	138.9502	165.66	16.12329	92.6597	112.35	17.52586	53.24745	78.96	32.56401
0.1	176.3967	187.72	6.032036	130.1062	144.49	9.954881	90.69395	81.18	-11.7196
1	213.8432	248.49	13.94295	167.5527	146.98	-13.9969	128.1404	103.34	-23.9989
10	251.2897	299.04	15.96788	204.9992	158.03	-29.7217	165.5869	121.92	-35.8161

Taking logarithm on both sides, Eq 12 can further be simplified as

$$\ln \dot{\epsilon} = \ln A_2 + \alpha \sigma - \frac{Q}{RT} \tag{Eq 13}$$

It should be noted that from Eq 13 the  $\alpha$  values at different test temperatures can be obtained from the linear fit of  $\ln \dot{\epsilon}$  and  $\sigma$  shown in Fig. 11(a).

As discussed in the preceding sections, generally the steady-state stress is used for the computation of  $Q_{HW}$  for DRV-type materials, whereas for materials exhibiting classical DRX, it is normal to use the peak stress (Ref 12, 23). Since, the material under present study, i.e., alloy AA2219 exhibits DRV, steady-state stress values which are observed at a strain of 0.5 are considered for the calculation of  $Q_{HW}$ . In the present study, the exponential law has been employed to obtain the value of stress multiplier ' $\alpha$ ' which is further used to compute  $Q_{HW}$  using the hyperbolic sine law.

Now at a particular temperature  $T$ , values of  $\ln \dot{\epsilon}$  and  $\sigma$  values taken at a true strain of 0.5 are plotted in Fig. 11(a). True stress-true strain data are used to obtain the plots. The value of  $\alpha$  (Eq 10, 11) is obtained from the slope of the linear fit of  $\ln \dot{\epsilon}$  and  $\sigma$  at a particular temperature. It is important to note that the value of the stress multiplier ( $\alpha$ ) is unique to each test temperature.

Now going back to Eq 11 which can also be rewritten (for all stresses) as:

$$\ln \dot{\epsilon} = \ln A + n \ln [\sinh(\alpha \sigma)] - \frac{Q}{RT} \tag{Eq 14}$$

From above equation, it can be seen that at constant  $T$ , the slope of linear fit of  $\ln \dot{\epsilon}$  and  $\ln [\sinh(\alpha \sigma)]$  gives the value of ' $n$ ', and similarly at constant  $\dot{\epsilon}$ , the slope of linear fit of  $\ln [\sinh(\alpha \sigma)]$  and  $1/T$  curves is taken as ' $S$ .' The aforementioned plots at all the temperatures and strain rates are presented in Fig. 11(b) and (c), respectively.

Finally, the value of  $Q$  for hot deformation is calculated by the following equation:

$$Q = R \left[ \frac{\partial \ln \dot{\epsilon}}{\partial \ln [\sinh(\alpha \sigma)]} \right]_T \cdot \left[ \frac{\partial \ln [\sinh(\alpha \sigma)]}{\partial (1/T)} \right]_{\dot{\epsilon}} = RnS \tag{Eq 15}$$

Since each pair of temperature and strain rate provides us with a different ' $Q$ ' value, the average value across all test temperatures and strain rate is computed and considered for further calculations.

The terms in Eq 10 are rearranged to get the Zener-Hollomon parameter ( $Z$ ) which is defined as (Ref 23, 31):

$$Z = \dot{\epsilon} \exp \left( \frac{Q_{HW}}{RT} \right) \tag{Eq 16}$$

The values of  $Z$  are calculated by substituting the previously computed average value of ' $Q$ ' and the corresponding temperatures ( $T$ ) and strain rates ( $\dot{\epsilon}$ ) in Eq 16.

Further taking logarithm on both the sides of Eq 12, we get

$$\ln Z = \ln A_E + \alpha \sigma \tag{Eq 17}$$

All the data points are plotted for  $\ln Z$  and  $\sigma$  (steady-state stress), and the slope of the linear fit provides the value for the constants  $A$  and  $\alpha$ . The linear fit of all data points is shown in Fig. 11(d).

Using the above calculated parameters as shown in Table 2, the constitutive equation has been established:

$$\dot{\epsilon} = 4.992 \times 10^{09} [\exp(0.06149\sigma)] \left[ \exp \left( \frac{-168.958 \times 10^3}{RT} \right) \right] \tag{Eq 18}$$

As already discussed in section 4.1, the strain hardening occurring in the material is in dynamic balance with mechanisms causing flow softening such as DRV and DRX during steady-state deformation. In case of aluminum alloys, the softening mechanism operative during hot working is DRV. To achieve a dynamic balance between strain hardening and DRV in aluminum alloy, an energy threshold must be overcome. The constant  $Q$  represents this threshold and often is termed as activation energy for hot deformation with  $Q$  value for the lattice self-diffusion in pure aluminum being 153 kJ/mol (Ref 32). The activation energy for hot deformation of aluminum AA2219 in the present study was found to be 169 kJ/mol. This value is higher than the self-diffusion activation energy value of pure aluminum indicating retardation in the flow softening mechanism (DRV) due to alloying element additions as previously discussed in the section on physical significance of  $Q$ . The value 169 kJ/mol compares reasonably well with the values established for other grades of aluminum alloys as presented in Table 3.

## 5. Validation of the Constitutive Equation

It is important to validate the constitutive equation from the point of view of its applicability. This is done by calculating the flow stress values ( $\sigma$ ) at a given deformation temperature ( $T$ ) and strain rate ( $\dot{\epsilon}$ ) using the derived constitutive equation and

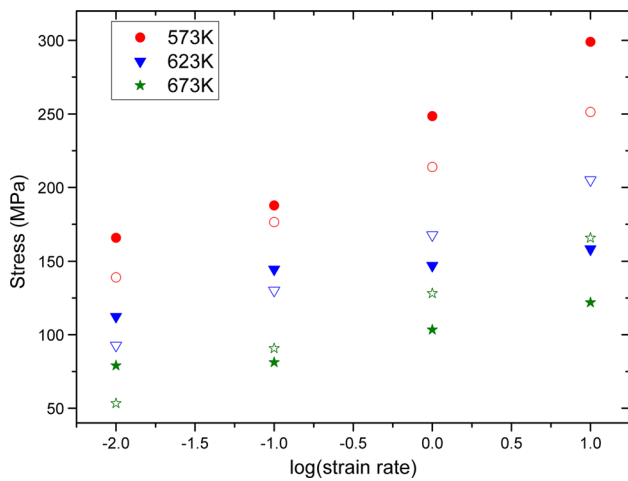


**Fig. 12** Comparison between calculated flow stress using the derived constitutive equation and the measured flow stress values in the temperature range 300–400 °C (573–673 K) and strain rate range (0.01–10 s<sup>-1</sup>). The hollow symbols are the calculated stress values while the solid symbols are measured stress values

comparing it with the measured values. The derived constitutive equation (Eq 18) is rewritten as

$$\sigma = \left( \ln \dot{\epsilon} + \frac{168958}{RT} - \ln(4.992 \times 10^9) \right) / 0.06149 \quad (\text{Eq 19})$$

For the purpose of validation, the comparison between the measured and calculated flow stress values is made in the temperature range 300–400 °C and strain rate range 0.01–10 s<sup>-1</sup> at a strain of 0.5. Table 4 and Fig. 12 show that the calculated and measured stress values compare well with low percentage of error ( $\pm 6$ –35%) in the chosen temperature and strain rate range. At higher deformation temperatures of 450 and 500 °C, the error is found to be more with the calculated stress values higher than the measured values. This can be attributed to severe flow softening observed in aluminum at high temperatures.

## 6. Conclusions

The hot working characteristics of AA2219 aluminum alloy were studied using isothermal uniaxial compression tests over the temperature range 300–500 °C and in the strain rate range 0.001–100 s<sup>-1</sup>. The following are the conclusions from this study.

1. Flow stress curves show only a gradual softening at all temperatures and strain rates except at 300 °C where strain hardening was followed by severe flow softening. This indicated occurrence of dynamic recovery as the principal restoration mechanism.
2. The processing map was used to identify regions of microstructural instability. The observed microstructures of compression tested specimens further validated the occurrence of these regions. The maps reveal two stable domains, viz. Domain I occurring at high temperature (370–500 °C) and low strain rates (0.001–0.01 s<sup>-1</sup>) and another Domain II at high temperature (370–500 °C) and high strain rates (0.32–10 s<sup>-1</sup>).

3. Optimum processing parameters (temperature 450 °C, strain rate 0.001 s<sup>-1</sup>) which render a fully reconstituted microstructure with no inhomogeneities were proposed, based on the processing map and observed microstructures.
4. Activation energy for the hot working of AA2219 was computed (169 kJ/mol) and found to be higher than the activation energy for self-diffusion of pure aluminum (153 kJ/mol).
5. The constitutive relationship for the hot deformation of AA2219 was established as:

$$\dot{\epsilon} = 4.992 \times 10^{09} [\exp(0.06149\sigma)] \left[ \exp\left(\frac{-168.958 \times 10^3}{RT}\right) \right]$$

## References

1. J. Zhang, B. Chen, and B. Zhang, Effect of Initial Microstructure on the Hot Compression Deformation Behaviour of a 2219 Aluminium Alloy, *Mater. Des.*, 2012, **34**, p 15–21
2. S.G. Pantelakis and N.D. Alexopoulos, Assessment of the Ability of Conventional and Advanced Wrought Aluminium Alloys for Mechanical Performance in Light-Weight Applications, *Mater. Des.*, 2008, **29**, p 80–91
3. N. Nayan, N.P. Gurao, S.V.S. Narayana Murty, A.K. Jha, B. Pant, S.C. Sharma, and K.M. George, Microstructure and Micro-Texture Evolution During Large Strain Deformation of an Aluminium-Copper-Lithium Alloy AA2195, *Mater. Des.*, 2015, **65**, p 862–868
4. H.J. Frost and M.F. Ashby, *Deformation Mechanism Maps, The Plasticity and Creep of Metals and Ceramics*, Pergamon Press, London, 1982
5. R. Raj, Development of a Processing Map for Use in Warm Forming and Hot Forming Process, *Metall. Trans. A*, 1981, **12**, p 1089–1097
6. S.L. Semiatin and G.D. Lahoti, The Occurrence of Shear Bands in Isothermal Hot Forging, *Metall. Trans. A*, 1992, **13**, p 275–288
7. G.E. Dieter, *Metals Hand Book*, 9th ed., vol. 14, American Society for Metals, Metals Park, OH, 1988, p 363–372
8. S.L. Semiatin and J.J. Jonas, *Formability and Workability of Metals: Plastic Instability and Flow Localization*, American Society for Metals, Metals park, Ohio, 1984
9. Y.V.R.K. Prasad, H.L. Gegel, S.M. Doraivelu, J.C. Malas, J.T. Morgan, K.A. Lark, and D.R. Barker, Modeling of Dynamic Material Behaviour in Hot Deformation: Forging of Ti-6242, *Metall. Trans. A*, 1984, **15A**, p 1883–1892
10. H.L. Gegel, J.C. Malas, S.M. Doraivelu, and V.A. Shende, *Modeling Techniques Used In Forging Process Design, Metals Handbook, Forming and Forging*, vol. 14, ASM International, Metals Park, OH, 1988, p 417–438
11. J.M. Alexander, *Mapping Dynamic Material Behaviour in Modeling of Hot Deformation of Steels*, J.G. Lenard, Ed., Springer, Berlin, 1989, p 101–115
12. H.J. McQueen, Elevated Temperature Deformation at Forming Rates of 10<sup>-2</sup>–10<sup>2</sup> s<sup>-1</sup>, *Metall. Mater. Trans. A*, 2002, **33A**, p 345–362
13. R. Kaibyshev, O. Sitdikov, I. Mazurina, and D.R. Leuser, Deformation Behaviour of 2219 Al Alloy, *Mater. Sci. Eng. A*, 2002, **34**, p 104–113
14. H. Ziegler, *Progress in Solid Mechanics*, I.N. Sneddon and R. Hill, Ed., Wiley, New York, NY, 1965, p 91–193
15. S.V.S. Narayana Murty, M.S. Sarma, and B. Nageswara Rao, On the Evaluation of Efficiency Parameter in Processing Maps, *Metall. Mater. Trans. A*, 1997, **28A**, p 1581–1582
16. S.V.S. Narayana Murty, B. Nageswara Rao, and B.P. Kashyap, Instability Criteria for Hot Deformation of Materials, *Int. Mater. Rev.*, 2000, **45**, p 15–26
17. S.V.S. Narayana Murty and B. Nageswara Rao, Ziegler's Criterion on the Instability Regions in Processing Maps, *J. Mater. Sci. Lett.*, 1998, **17**, p 1203–1205
18. S.V.S. Narayana Murty and B. Nageswara Rao, On the Dynamic Material Model for the Hot Deformation of Materials, *J. Mater. Sci. Lett.*, 1999, **18**, p 1757–1758

19. S.V.S. Narayana Murty and B. NageswaraRao, On the Development of Instability Criteria During Hot Working with Reference to IN 718, *Mater. Sci. Eng. A*, 1998, **254**, p 76–82
20. S.V.S. Narayana Murty, B. Nageswara Rao, and B.P. Kashyap, Development and Validation of a Processing Map for AFNOR 7020 Aluminum Alloy, *Mater. Sci. Technol.*, 2004, **20**, p 772–782
21. C.M. Sellars and WJMcG Tegart, Hot Workability, *Int. Metall. Rev.*, 1972, **17**, p 1–24 ((Review 158))
22. J. Jonas, C.M. Sellars, and WJMcG Tegart, Strength and Structure Under Hot-Working Conditions, *Metall. Rev.*, 1972, **14**, p 1–24 ((Review 130))
23. H.J. McQueen and N.D. Ryan, Constitutive Analysis in Hot Working, *Mater. Sci. Eng. A*, 2002, **322**, p 43–63
24. C. Shi and X.-G. Chen, Evolution of Activation Energies for Hot Deformation of 7150 Aluminum Alloys with Various Zr and V Additions, *Mater. Sci. Eng. A*, 2016, **650**, p 197–209
25. C. Shi, W. Mao, and X.-G. Chen, Evolution of Activation Energy During Hot Deformation of AA7150 Aluminum Alloy, *Mater. Sci. Eng. A*, 2013, **571**, p 83–91
26. T. Sakai, A. Belyakov, R. Kaibyshev, H. Miura, and J.J. Jonas, Dynamic and Post-Dynamic Recrystallization Under Hot, Cold and Severe Plastic Deformation Conditions, *Prog. Mater. Sci.*, 2014, **60**, p 130–207
27. R. Kaibyshev, I. Mazurina, and O. Sitdikov, Geometric Dynamic Recrystallization in an AA2219 Alloy Deformed to Large Strains at an Elevated Temperature, *Mater. Sci. Forum*, 2004, **467–470**, p 1199–1204
28. N. Nayan, N.P. Gurao, S.V.S. Narayana Murty, A.K. Jha, B. Pant, and K.M. George, Microstructure and Micro-Texture Evolution During Large Strain Deformation of Inconel Alloy IN718, *Mater. Charact.*, 2015, **110**, p 236–241
29. E.T. George and D.S. MacKenzie, Ed., *Handbook of Aluminium: Volume 2: Alloy Production and Materials Manufacturing*, Marcel Dekker Inc., New York, 2003, p 213–214
30. R. Kaibyshev, I. Kazakulov, D. Gromov, F. Musin, D.R. Leuser, and T.G. Nieh, Superplasticity in a 2219 Aluminium Alloy, *Scr. Mater.*, 2001, **44**, p 2411–2417
31. C. Zener and J.H. Hollomon, Effect of Strain Rate Upon Plastic Flow of Steel, *J. Appl. Phys.*, 1944, **15**, p 22
32. T. Sheppard, Ed., *Extrusion of Aluminium Alloys*, 1st ed., Springer Science+Business Media, Dordrecht, 1999, p 135
33. K.E. Tello, A.P. Gerlich, and P.F. Mendez, Constants for Hot Deformation Constitutive Models for Recent Experimental Data, *Sci. Technol. Weld. Join.*, 2010, **15**, p 260–266
34. E. Cerri, E. Evangelista, A. Forcellese, and H.J. McQueen, Comparative Hot Workability of 7012 and 7075 Alloys After Different Pre-Treatments, *Mater. Sci. Eng. A*, 1995, **197**, p 181–198